Hydroclimatic Controls on the Means and Variability of Vegetation Phenology and Carbon Uptake

R. D. KOSTER

Global Modeling and Assimilation Office, NASA Goddard Space Flight Center, Greenbelt, Maryland

G. K. WALKER

Global Modeling and Assimilation Office, NASA Goddard Space Flight Center, Greenbelt, and Science Systems and Applications, Inc., Lanham, Maryland

G. J. COLLATZ

Biospheric Sciences Laboratory, NASA Goddard Space Flight Center, Greenbelt, Maryland

P. E. THORNTON

Environmental Sciences Division and Climate Change Science Institute, Oak Ridge National Laboratory, Oak Ridge, Tennessee

(Manuscript received 8 August 2013, in final form 14 February 2014)

ABSTRACT

Long-term, global offline (land only) simulations with a dynamic vegetation phenology model are used to examine the control of hydroclimate over vegetation-related quantities. First, with a control simulation, the model is shown to capture successfully (though with some bias) key observed relationships between hydroclimate and the spatial and temporal variations of phenological expression. In subsequent simulations, the model shows that (i) the global spatial variation of seasonal phenological maxima is controlled mostly by hydroclimate, irrespective of distributions in vegetation type; (ii) the occurrence of high interannual moisture-related phenological variability in grassland areas is determined by hydroclimate rather than by the specific properties of grassland; and (iii) hydroclimatic means and variability have a corresponding impact on the spatial and temporal distributions of gross primary productivity (GPP).

1. Introduction

Recognition that the earth's energy and water cycles are intrinsically entwined is longstanding (e.g., Budyko 1974). The land surface energy and water balances both feature evapotranspiration as a dominant term, and the generation of rainfall (a key component of the water cycle) has a profound effect on the heat budget of the atmosphere. The inseparability of the energy and water cycles underlies their joint treatment in numerous analyses (e.g., Trenberth et al. 2011) and the formation of international research projects addressing their linkage, such as the Global Energy and Water Cycle Experiment [GEWEX, part of the World Climate Research Programme (WCRP)].

The earth's carbon cycle is in turn intrinsically entwined with the energy and water cycles. Vegetation health (and associated carbon uptake) is affected by water availability; deserts, for example, tend not to be carbon sinks. Conversely, carbon affects the water and energy cycles; the transpiration of water from vegetation and the associated cooling of the land surface are in large part controlled by the efficiency of the vegetation's uptake of carbon dioxide (e.g., Berry et al. 2010), and the buildup of vegetation through carbon uptake has a direct impact on land surface albedo—how much of the sun's radiation is absorbed by the surface. Carbon dioxide is, of course, also a greenhouse gas. The basic connection between the surface fluxes of water, energy, and carbon is appropriately recognized in numerous

Corresponding author address: Randal Koster, Global Modeling and Assimilation Office, Code 610.1, NASA GSFC, Greenbelt, MD 20771.
E-mail: randal.d.koster@nasa.gov

DOI: 10.1175/JCLI-D-13-00477.1

© 2014 American Meteorological Society

studies (e.g., Leuning et al. 2004; Bowling et al. 2010), and it is a motivation for international research projects such as the Integrated Land Ecosystem–Atmosphere Processes Study (ILEAPS, another component of WCRP).

In this paper, we focus in particular on the carbon–water linkage at the land surface. A number of relevant studies in the literature have shared this focus. Using data collected at a number of flux tower sites in North America, Knapp and Smith (2001) provided a powerful, geographically diverse analysis of the connections between the surface water and carbon cycles—specifically, of the controls of precipitation means and variability on above-ground net primary production (ANPP). Their results show that carbon uptake by the land surface is indeed strongly regulated by precipitation characteristics, with maximum uptake related strongly to precipitation amount and with the interannual variability of the uptake maximized in grassland areas, where both precipitation variability and vegetation cover are adequately high. Remotely sensed measurements of vegetation properties allow for an even more comprehensive and large-scale analysis of connections between carbon and climatic variables, including precipitation (e.g., Fang et al. 2005; Ichii et at. 2002; Jahan and Gan 2011). In a recent global analysis, Zeng et al. (2013) uncovered strong relationships between the interannual variations contained in a multidecadal normalized difference vegetation index (NDVI) dataset (an indicator of green leaf area) and antecedent precipitation levels, particularly in temperate and tropical grasslands.

A modeling framework is a natural venue for studying the connections between carbon and water. Wang and Eltahir (2000), using a simple coupled biosphere–atmosphere model, showed how the interaction between vegetation and precipitation can lead to multiple equilibria for vegetation state. Zeng et al. (1999) showed, again with a simple coupled model, how vegetation–climate interactions may affect the nature of precipitation variability in the Sahel. Puma et al. (2013) used a modeling framework to compare the impacts of meteorological variability and phenological variability on the simulation of surface moisture and carbon fluxes. Complex and relatively complete models of vegetation behavior, models that indeed tie together explicitly the interactions between carbon, energy, and water fluxes at the land surface and accordingly allow the prediction of vegetation state, are arguably the new state of the art in numerical climate modeling. Sellers et al. (1997) pointed to the explicit treatment of carbon as a logical step in the evolution of land surface treatments in Earth System models; dynamic vegetation models (DVMs) following this evolutionary path are already being used at major climate modeling centers (e.g., Lawrence et al. 2011; Krinner et al. 2005; Boussetta et al. 2013; Dunne et al. 2013).

An advantage of using a modeling framework for carbon–water studies is the potential for doing unique analyses that isolate and illustrate the mechanisms that control the transfers of water and carbon across the land surface. Carefully formulated modifications of a physical process treatment or of a variable that forces it can be imposed, and the resulting impacts on surface fluxes can be quantified and analyzed, thereby elucidating the role of the process examined. A second important advantage of such models is their ability to provide data fields that are otherwise unattainable, at least not directly. Gross primary productivity (GPP), for example, can only be measured directly at a limited number of flux tower sites, and satellite-based estimates of GPP are at best indirect, relying on their own model assumptions. A DVM, if driven with observations-based meteorological forcing, can potentially produce estimates of GPP at high spatial and temporal resolution across the globe. Such estimates would be biased relative to nature, of course, owing to deficiencies in model formulation and forcing data; still, if care is given to their interpretation, the estimates do have scientific value.

Both of these advantages come into play in the present paper, in which we use the dynamic phenology component of an established DVM together with the water and energy balance framework of a hydrology-focused land surface model (LSM) to characterize, on a global scale, the controls of precipitation means and variability on GPP: both on its spatial distribution and on its temporal variability across the globe. The modeling system used (described in section 2) is, indeed, found to be effective in capturing the key hydroclimatic controls on phenology that operate in nature (as demonstrated in section 3). The simulated GPP distributions from the thus-validated system are analyzed jointly with global precipitation data in section 4. The model experiments provide new insights into the relative impacts of precipitation means, precipitation variability, and vegetation type in determining GPP distributions.

2. Dynamic phenology model

The dynamic phenology model used in this study is in essence a merger of the carbon (i.e., prognostic biogeochemistry) physics of the National Center for Atmospheric Research (NCAR)–U.S. Department of Energy (DOE) Community Land Model, version 4 (CLM4) dynamic vegetation model (Oleson et al. 2010) with the energy and water balance formulations of the National Aeronautics and Space Administration (NASA) Global Modeling and Assimilation Office (GMAO) catchment LSM (Koster et al. 2000). We provide here a brief description of these two components and the

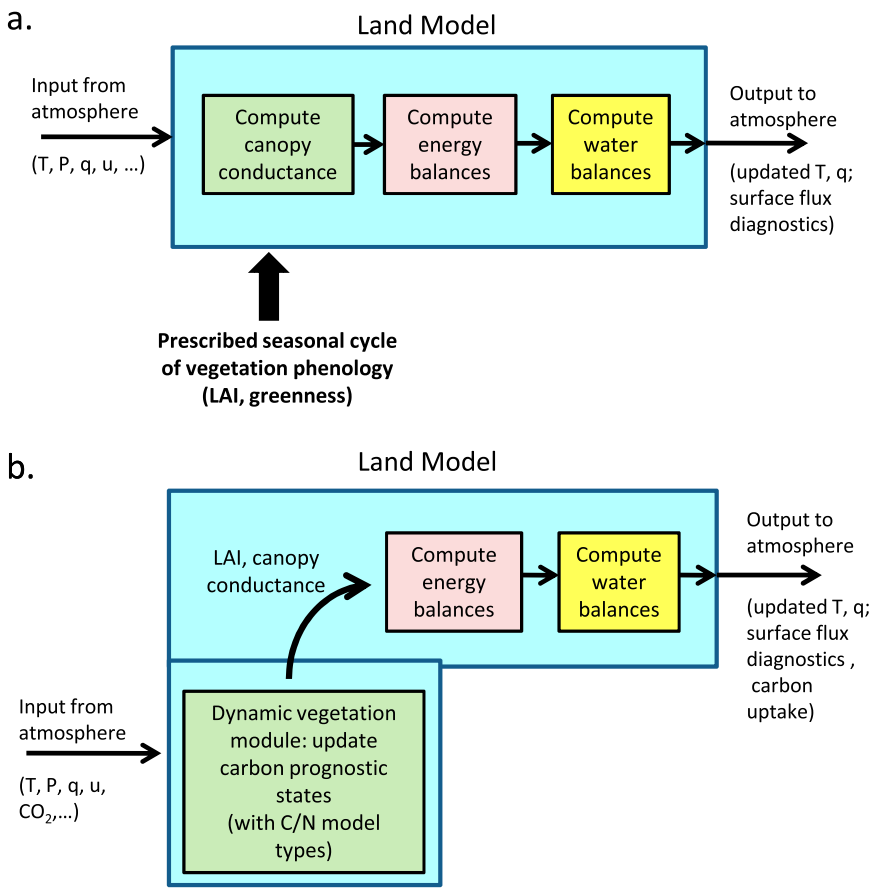

FIG. 1. Schematic of flux computations in (a) the original catchment LSM and (b) the merged model, Catchment-CN.

technique used to merge them into a new model: the catchment LSM with carbon and nitrogen physics (Catchment-CN LSM).

The NCAR–DOE CLM4 represents prognostic coupled energy, water, carbon, and nitrogen cycles in a framework that permits global-scale as well as regional and site-level simulation. The global-scale parameterization used here includes specification of subgrid heterogeneity in plant functional type (PFT) distributions, with multiple PFTs assigned fractional area coverage within each grid cell, where they compete with one another for available soil moisture and mineral nitrogen resources. In this prescribed biogeography mode, the fractional areas occupied by individual PFTs do not change, but vegetation growth, soil heterotrophic activity, carbon stocks, and other ecosystem states (e.g., leaf area index) do vary prognostically (Thornton et al. 2009).

The GMAO catchment land surface model is a state-of-the-art surface energy and water budget model designed for use with global Earth System models. As with most other LSMs, the catchment LSM employs complex treatments of land surface flux generation, tying the efficiency of evaporation and runoff generation to the moisture and temperature states of the land surface, and it includes parameterizations of vegetation impacts on transpiration, canopy interception, albedo, and surface roughness. Relatively unique to the catchment LSM is its treatment of the subgrid variability of soil moisture and temperature, which is explicitly tied to a description of the topographic variability in the region modeled: in the catchment LSM, valley bottoms within a given grid element are explicitly modeled as being wetter and the hilltops are explicitly modeled as being drier. Runoff and evaporation are calculated independently in the different hydrological regimes, using regime-specific physics.

In essence, in merging the two models, we retain the catchment LSM's energy and water balance calculation framework while using the NCAR–DOE CLM4 carbon balance calculations. The approach is illustrated in Fig. 1. In the original catchment LSM (Fig. 1a), the model uses forcing from the atmosphere along with

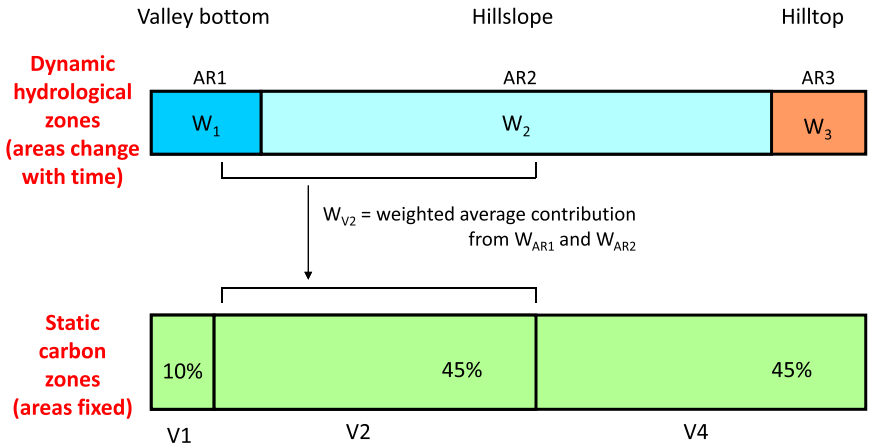

FIG. 2. Schematic of independent vegetation (carbon) treatments in topographically defined vegetation zones. Three static vegetation zones are defined, with independent carbon prognostic variables in each. The W_1, W_2, and W_3 are soil moisture states in the three dynamically varying hydrological zones (with time-varying areas AR1, AR2, and AR3); weighted averages of these states (e.g., W_{V2}, as shown in the figure) and corresponding weighed temperature states are passed down to the carbon physics calculations for the different vegetation zones. Weighted averages of vegetation zone quantities (e.g., canopy conductance) are similarly passed back to the hydrological zones.

prescribed vegetation phenology [leaf area index (LAI) and greenness fraction] and the current values of LSM temperature and moisture prognostic variables to compute the canopy conductance, the parameter describing the ease with which the plants transpire water. The canopy conductance, computed separately for each hydrological regime, is then used in each regime's energy balance and water balance calculations, which in turn provide the fluxes of heat and moisture to the atmosphere.

Figure 1b shows the approach used by the merged system, the Catchment-CN LSM. The atmospheric inputs are now fed first into the components of the NCAR–DOE model that update the carbon states and compute, as a matter of course, canopy conductances that reflect an explicit treatment of photosynthesis physics. These canopy conductances, along with the leaf area indices diagnosed from the new carbon prognostic variables, are fed into the energy and water balance calculations of the original catchment LSM. The output fluxes with the merged system include a net carbon flux.

The merger of the two models allows the Catchment-CN LSM to follow 19 distinct vegetation types, a significant increase from the 6 independent types followed with the original catchment LSM. Furthermore, the unique character of the original catchment LSM allows for the independent monitoring of carbon variables in the different topographically defined hydrological regimes. Figure 2 describes our methodology. Each land surface element is subdivided into three static vegetation (carbon) zones defined by topography, through analysis of the distribution of the compound topographic index (Moore et al. 1993). The first zone, covering a fixed 10% of the area, represents the valley bottoms; this zone tends to be generally wet. The second and third zones represent the lower (drier) hill slopes and upper (even drier) hill slopes, respectively. Through areal weighting, soil moisture and temperature information from the dynamically varying hydrological zones are combined for use by the carbon physics in the fixed vegetation zones, as indicated in the figure. Separate sets of carbon prognostic variables (associated with up to two coexisting PFTs) are followed in each vegetation zone, and thus each vegetation zone generates its own manifestation of phenology.

The fractions for the three static vegetation zones (10%, 45%, and 45%) are arbitrarily chosen nominal values. Note that in comparatively flat areas, the hydrological states of the three vegetation zones will be similar, and thus the phenology generated in each zone will be about the same. Hydrological distinctions between the vegetation zones and thus phenological distinctions between the zones will necessarily be larger in areas with greater topographic variation. When examining the model results, we indeed find that in mountainous areas, green vegetation tends to be significantly denser in the valley bottoms.

Some additional modifications to the NCAR–DOE vegetation model were needed to optimize its performance in the GMAO system. To prevent some occasional

singular behavior—namely, the catastrophic shutdown of vegetation during cold spells and a resulting overgrowth of the vegetation during the subsequent growing season—we replaced a particular set of vegetation types (crop and temperate shrubs/grass) that feature a strong response to temperature stress by a mix of two different types: one that is seasonally deciduous and one that is not. Neither of the replacement types employs the temperature stress shutdown, though both respond to moisture stress. The proportion of the mix applied is defined by latitude, and the replacement is indeed limited to the latitude band 32°–42° in both hemispheres; outside of this latitudinal band, the number of coexisting PFTs in each static carbon zone remains limited to two. Note that this replacement in vegetation type mimics a simple removal of the temperature stress function from the original types, as the other physical aspects of the original and replacement types are essentially the same.

Also, we modified the NCAR–DOE vegetation physics to allow half of the new carbon assimilated by deciduous types to be displayed during the current year rather than in the following year, which brings certain measures of our interannually varying phenology (in particular, the correlation between FPAR and antecedent precipitation) more in line with observations. The literature indeed supports the idea that for some vegetation types, assimilated carbon is displayed during the current year rather than stored for display in the following year (e.g., Kobe 1997). Finally, whereas the NCAR–DOE vegetation model uses the previous year's annual mean temperature to determine certain onset triggers, we use the more stable climatological mean temperature. This choice is more in line with the original intent of the NCAR–DOE model's phenology scheme, a scheme that originally used a multiyear average (White et al. 1997). The NCAR–DOE model switched to a single-year average for logistical rather than scientific reasons.

In our main (''control'') application of the model, the prescribed distributions of vegetation type follow those used by the default 0.5° × 0.5° version of CLM4 (Oleson et al. 2010). Vegetation phenology and carbon states, however, evolve freely. The model is run globally offline (i.e., disconnected from an atmospheric model) on high-resolution catchments (roughly 20–30 km in size) over the period 1948–2008, using the observations-based meteorological forcing of Sheffield et al. (2006). The simulation first loops over this period 57 times to spin up the carbon storage reservoirs, resulting in 3477 years of spinup—on the order needed to bring about the equilibration of certain biome types (Shi et al. 2013). (Note that we also utilized the CLM4 ''accelerated decomposition'' option for the first 600 years, which reduces somewhat the required spinup time.) The 58th cycle of 61 yr is analyzed here.

Our focus in this paper is on the connections between hydroclimate and vegetation. Given that the historical precipitation record should be more accurate at coarser spatial scales, the output data examined (phenological variables, carbon fluxes, etc.) are aggregated to 2° × 2.5° for processing.

3. Evaluation against observations

To test the realism of the model's connections between hydroclimate and vegetation variables, we focus on two distinct aspects of global phenological expression: the global spatial pattern of long-term phenological means and the interannual variability of phenology at a given location. These are discussed in turn following a brief description of the observations.

a. Observations used

We examine satellite-based products of the normalized difference vegetation index (NDVI) and fraction of absorbed photosynthetically active radiation (FPAR), both of which increase with green vegetation cover. The NDVI data are a subset of the latest version of the Global Inventory Modeling and Mapping Studies (GIMMS) data (Tucker et al. 2005). The data's native resolution is semiweekly at 8 km and span the period July 1981–present. For our analyses, we aggregate these data to a 2.5° × 2.5° monthly resolution for the period 1982–2010. The data are derived from the Advanced Very High Resolution Radiometer (AVHRR) instrument with known limitations compared to the more advanced Moderate Resolution Imaging Spectroradiometer (MODIS) instrument (Kaufman et al. 1998). However, the longer temporal coverage of GIMMS relative to MODIS (29 versus 11 yr) and the good correspondence between their measurements (Tucker et al. 2005; Beck et al. 2011) makes it well suited to the analysis presented here.

The FPAR data are derived directly from the NDVI data using the method of Los et al. (2000). The method combines the NDVI-based FPAR estimation technique of Sellers et al. (1996) with that of Choudhury (1987) and Goward and Huemmrich (1992); the combination provides estimates that are well behaved relative to available in situ observations. The relationship between NDVI and FPAR underlying this combined approach is monotonic but nonlinear. Note that it is also somewhat vegetation dependent, so the conversion of global NDVI data to global FPAR data requires a global field of vegetation types. Thirteen years of FPAR data are available, spanning the period 1997–2009.

As will be seen below, the sensitivities of the NDVI and FPAR data to hydroclimatic variation are similar in many ways. Both are worth illustrating here. The NDVI values are constructed directly from spectral reflectance measurements and thus represent a raw form of the observations. While the construction of the FPAR values requires some additional assumptions regarding vegetation behavior, FPAR has the distinct advantage of representing a physically meaningful phenological variable, one that can be compared directly to output from the Catchment-CN model.

The global precipitation data used here consist of monthly precipitation totals for 1979–present at 2.5° × 2.5° resolution, produced by the Global Precipitation Climatology Project as part of their version 2 satellite-gauge dataset (Adler et al. 2003; see also ftp://precip.gsfc.nasa.gov/pub/gpcp-v2.2/doc/V2.2_doc.pdf). Satellite-based data contributing to the product, in varying capacities and over various periods and regions, include Special Sensor Microwave Imager (SSM/I) passive microwave estimates, Television Infrared Observation Satellite (TIROS) Operational Vertical Sounder (TOVS) estimates, and the adjusted Geostationary Operational Environmental Satellite (GOES) precipitation index (Adler et al. 1994). A wealth of surface rain gauges is used to adjust the multisensor precipitation estimates over land. Hall et al. (2006) provide background on the accuracy of the GPCP product; of note is the higher uncertainty of the product over mountains, deserts, high latitudes, and undeveloped areas due in large part to a lower density of rain gauges.

b. *Impact of hydrological variations on the mean spatial distributions of phenological variables*

To deal with the fact that NDVI shows significant seasonal variability, with different regions having different peak months for the index, we examine a quantity we will call $\mathrm{NDVI_{max}}$. We compute, at each 2.5° × 2.5° grid cell, the average seasonal cycle of NDVI from the GIMMS data and then identify the month for which the average NDVI is highest. $\mathrm{NDVI_{max}}$ is set to the average value for the 3-month period centered on this peak month. (Note that, under this definition, the values for $\mathrm{NDVI_{max}}$ in adjacent grid cells may be taken from different 3-month periods.) Figure 3a shows the global distribution of $\mathrm{NDVI_{max}}$ as derived from the spatially aggregated GIMMS data. The distribution mirrors known vegetation distributions, with large values in tropical, deciduous, and boreal forests; intermediate values in grassland and shrubland areas; and small values in the deserts.

We can use statistical analysis to relate the spatial distribution of NDVI to that of various meteorological quantities in order to determine which quantities are related to (and thus may help determine) the NDVI distribution. The first five bars in Fig. 4a show the square of the spatial correlation (r^2, across land surface grid cells) of $\mathrm{NDVI_{max}}$ in Fig. 3a with annual mean precipitation, the standard deviation (across years) of annual precipitation totals, annual mean air temperature, absolute value of the warm-season temperature deviation from an assumed optimal value, and annual mean net radiation. The base-10 logarithms of the precipitation quantities are in fact used here. Temperature and net radiation information are derived from the full period of the Sheffield et al. (2006) dataset. The outgoing longwave component of the net radiation is estimated using the surface air temperature in that dataset. The temperature deviation is computed as $|T_w - T_{\mathrm{opt}}|$, where T_w is the average monthly temperature of the climatologically warmest month of the grid cell being processed and T_{opt} is equal to 292 K, the temperature that (through testing) provides the highest possible value for the fourth bar in Fig. 4.

The salient result from the figure is the dominance of the two precipitation quantities in determining the spatial structure of NDVI. While the deviation of temperature from the fitted optimal value of 292 K is also apparently important, together the two precipitation quantities are seen to explain most of the variance in $\mathrm{NDVI_{max}}$: results of multiple regression analysis of $\mathrm{NDVI_{max}}$ on combinations of variables show that the mean and standard deviation of precipitation together produce an r^2 of about 0.55 (sixth bar), whereas the r^2 obtained when all variables, including the temperature deviations, are considered is about 0.65 (seventh bar). (Note that there is apparently some redundant information in the precipitation and $|T_w - T_{\mathrm{opt}}|$ fields.) The relative heights of the sixth and seventh bars in Fig. 4a underline the importance of hydroclimate in determining the spatial distribution of phenological maxima.

Figure 5a shows more directly how $\mathrm{NDVI_{max}}$ is related to precipitation means and variability. Each dot in Fig. 5a corresponds to a 2.5° × 2.5° land grid cell. The size and color of the dot is determined by the local value of $\mathrm{NDVI_{max}}$, as indicated by the legend. The dot's abscissa is determined by the mean annual precipitation at that grid cell, and its ordinate refers to the interannual variability of precipitation there (note the logarithmic scales). The precipitation and NDVI quantities are computed over consistent time periods; for example, if a grid cell's peak NDVI, as computed from the GIMMS data for 1982–2010, occurs in July, then precipitation means and variances are computed from 19 September–August yearly totals starting with the total for the period September 1981–August 1982.

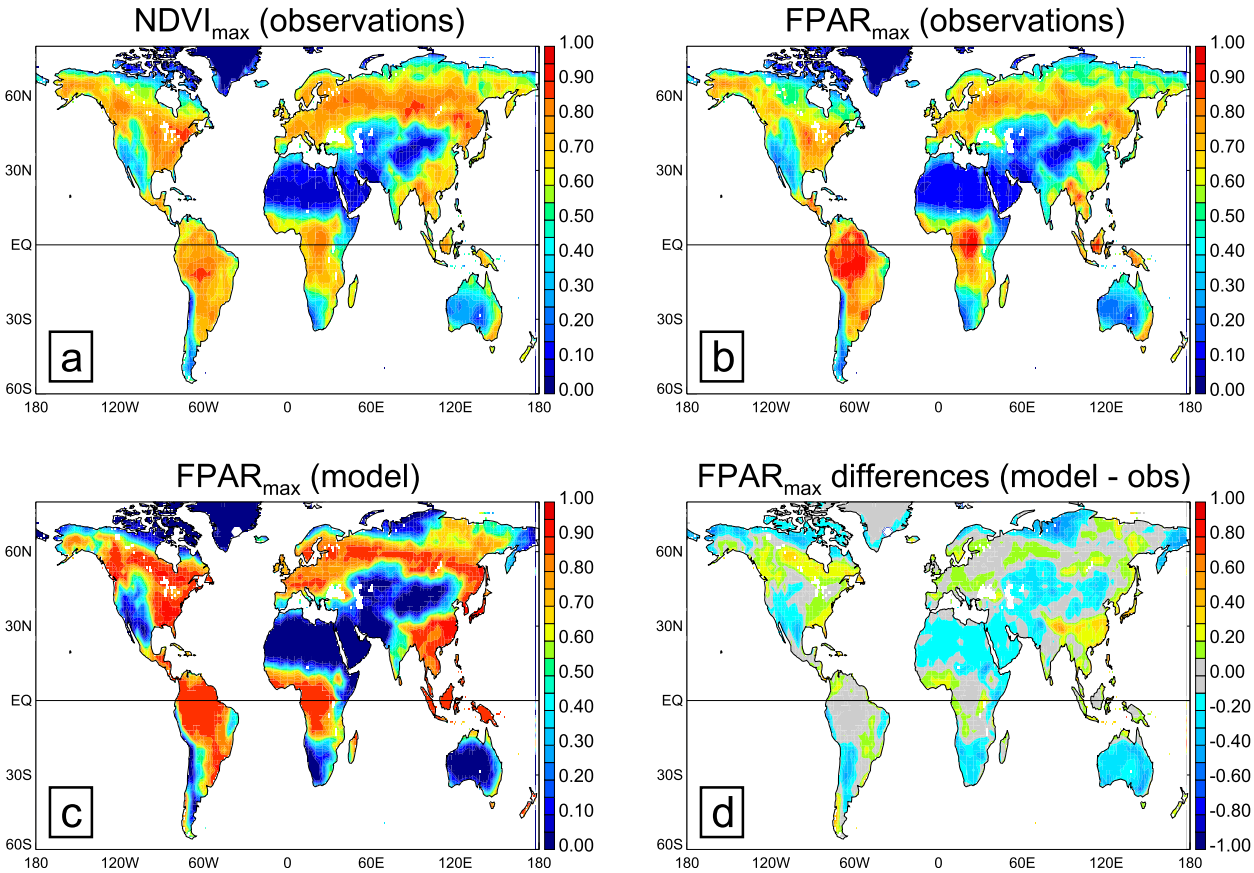

FIG. 3. (a) Distribution of average NDVI in peak NDVI season (the month for which the mean seasonal cycle of NDVI is maximized along with the preceding and following months), from GIMMS observations. The peak season varies with grid cell; see text for details. (b) As in (a), but for average FPAR in peak FPAR season, from GIMMS observations. (c) As in (a), but for average FPAR in peak FPAR season, from model simulation. (d) Difference between (c) and (b).

Two features of the scatterplot stand out. The first reflects an expected result: a minimum average precipitation must be achieved to attain moderately high $NDVI_{max}$ levels. The plot shows this minimum value to be roughly $1\,mm\,day^{-1}$; the dots to the left of this threshold (which include, of course, all desert points) show low values of $NDVI_{max}$. The second, and more intriguing, feature of the scatterplot is the tendency for $NDVI_{max}$ to decrease as the standard deviation of precipitation increases. This feature is illustrated more clearly in Fig. 5b, which shows a binned version of the scatterplot data; to generate this plot, an array of boxes is overlain on Fig. 5a, and the $NDVI_{max}$ values for the points within each box are averaged. For a given value of the mean precipitation, especially for values above $1\,mm\,day^{-1}$, $NDVI_{max}$ clearly tends to decrease with increasing σ_P. This presumably reflects the reduced ability of vegetation to flourish when the year-to-year supply of water is less stable.

We also examine in this context the analogous variable $FPAR_{max}$, the average value of a grid cell's FPAR for the 3-month period centered on the peak FPAR month, as determined from the local climatological cycle. Figure 3b shows the distribution of $FPAR_{max}$ as computed from the GIMMS data. As might be expected, given that FPAR in GIMMS is derived from NDVI, the spatial distributions in Figs. 3a,b are very similar, as are the spatial correlations with the meteorological forcing variables (Fig. 4b). Figures 5c,d show the precipitation-based scatterplots for the $FPAR_{max}$ values. Average water supply (mean precipitation) and water supply stability (σ_P) are seen to impose dual control over $FPAR_{max}$ as well. The sensitivity of FPAR to hydroclimate is, indeed, very similar to that of NDVI—again not an unexpected result, given the dependence of the FPAR data on NDVI.

How well does the Catchment-CN model perform? The model produces diagnostics for both the incident and absorbed photosynthetically active radiation; we take the ratio of these quantities to produce the model's FPAR values. Figure 3c shows the global distribution of simulated FPAR in the peak 3-month period; note that for a given location this peak period may differ from

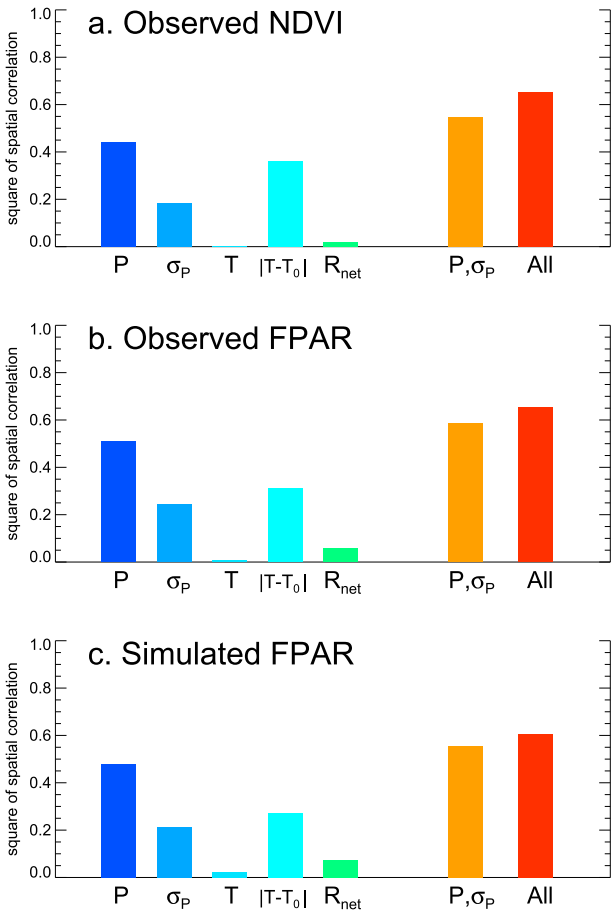

FIG. 4. (a) Square of the spatial correlation coefficient (over land grid cells) between observed NDVI and land surface forcing variables: the logarithm of the mean annual precipitation (P), the logarithm of the standard deviation of annual precipitation (σ_P), mean annual air temperature (T), the deviation of average warmest month temperature from an assumed optimum (see text), and mean annual net radiation (R_{net}). The final two bars show the square of the correlation coefficient obtained from the multiple regression of NDVI against (i) precipitation mean and standard deviation and (ii) all five quantities. As in (a), but (b) for observed FPAR and (c) for modeled FPAR.

that for the observations. Two features of the simulated FPAR distribution stand out. First, the simulated spatial patterns in Fig. 3c agree well with the observed patterns in Fig. 3b; the model properly captures, at least to first order, the global spatial distribution of FPAR. Second, there are, nonetheless, apparent biases in the simulated FPAR values, with the highest simulated values being too large and the lowest being too small. These biases are shown clearly in the difference map in Fig. 3d. Such biases presumably reflect deficiencies in the model, though they may also stem partially from limitations in the forcing data or in the observational FPAR values themselves: consider, for example, the observations-based FPAR values of about 0.1 in the Sahara and Gobi deserts, which are probably too large.

Additional evaluation of the model's simulation of FPAR, particularly of its seasonal cycle, is provided in Fig. 6. Mean seasonal cycles of FPAR were computed at each location from the observations-based GIMMS estimates and from the model simulations. For the purposes of the plot, the month in the cycle for which the FPAR value is first considered "large" (i.e., is in the upper half of the full range) in the climb toward the peak FPAR month is loosely defined as the leaf onset month of the cycle. Note that the FPAR observations have monthly resolution, prohibiting a more precise characterization of the onset date. Overall, the simulated onset months (Fig. 6b) agree reasonably well with the observed values (Fig. 6a), though some mismatches do appear (e.g., in southern Australia and Southeast Asia). The "season length"—that is, the number of months in the mean seasonal cycle for which FPAR lies in the upper half of its range—is plotted for the observations in Fig. 6c and for the model results in Fig. 6d. Here the model is seen to overestimate the season length, often by a month or two. We note that the date of leaf fall in the model is assumed to be controlled by solar declination and is thus effectively prescribed; the prescribed leaf-fall dates could potentially be modified in future studies based on the GIMMS data.

As discussed in section 2, the carbon physics of the model used here, the Catchment-CN model, are essentially the same as those in the NCAR–DOE CLM4 prognostic biogeochemistry model. These carbon physics were, in fact, tested extensively against observations (Randerson et al. 2009) as part of the Carbon-Land Model Intercomparison Project (C-LAMP). In one C-LAMP analysis, for example, the modeled carbon physics were found to produce a late (~2 month) maximum in LAI relative to LAIs inferred from MODIS; as expected, a similar analysis with the Catchment-CN results (not shown here) shows much the same late bias. It is reasonable to expect that, in general, the biases identified by Randerson et al. (2009) also apply here and that, while some biases may relate to limitations in the observations, most probably originate from model deficiencies. The presence of bias, generally inescapable in modeling studies, must be kept in mind throughout our analysis.

Turning now to the simulated response of FPAR to hydroclimatic variation in the Catchment-CN model, we show in Fig. 4c the square of the spatial correlation of simulated FPAR with meteorological forcing variables. The values found for the model agree well with

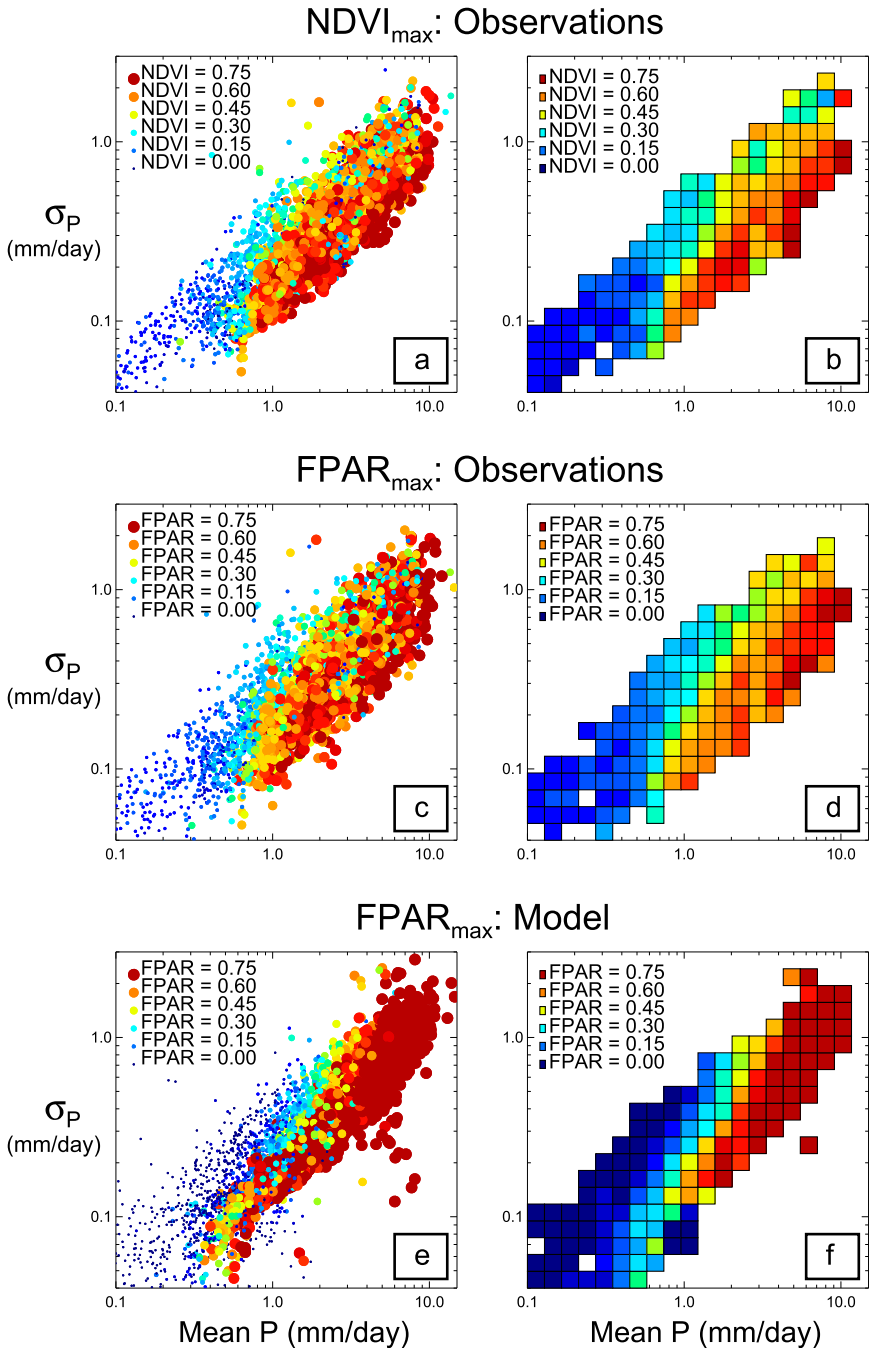

FIG. 5. (a) Average GIMMS NDVI in peak NDVI season as a function of the mean annual precipitation (x coordinate) and the standard deviation of annual precipitation (y coordinate). Each dot represents a single land grid cell. (b) As in (a), but with the individual values in the scatterplot averaged over bins. At least five dots must lie within a bin for the binned value to be plotted. (c),(d) As in (a),(b), but for GIMMS FPAR data. (e),(f) As in (a),(b), but for model-simulated FPAR data.

the corresponding values found for observed FPAR (Fig. 4b). The simulated r^2 values with the temperature and net radiation variables are slightly higher, but these values are still small compared to that for the combined effect of the precipitation variables. Figure 4c shows that, in strong agreement with the observations, variations in hydroclimate explain most of the FPAR variability seen in the model.

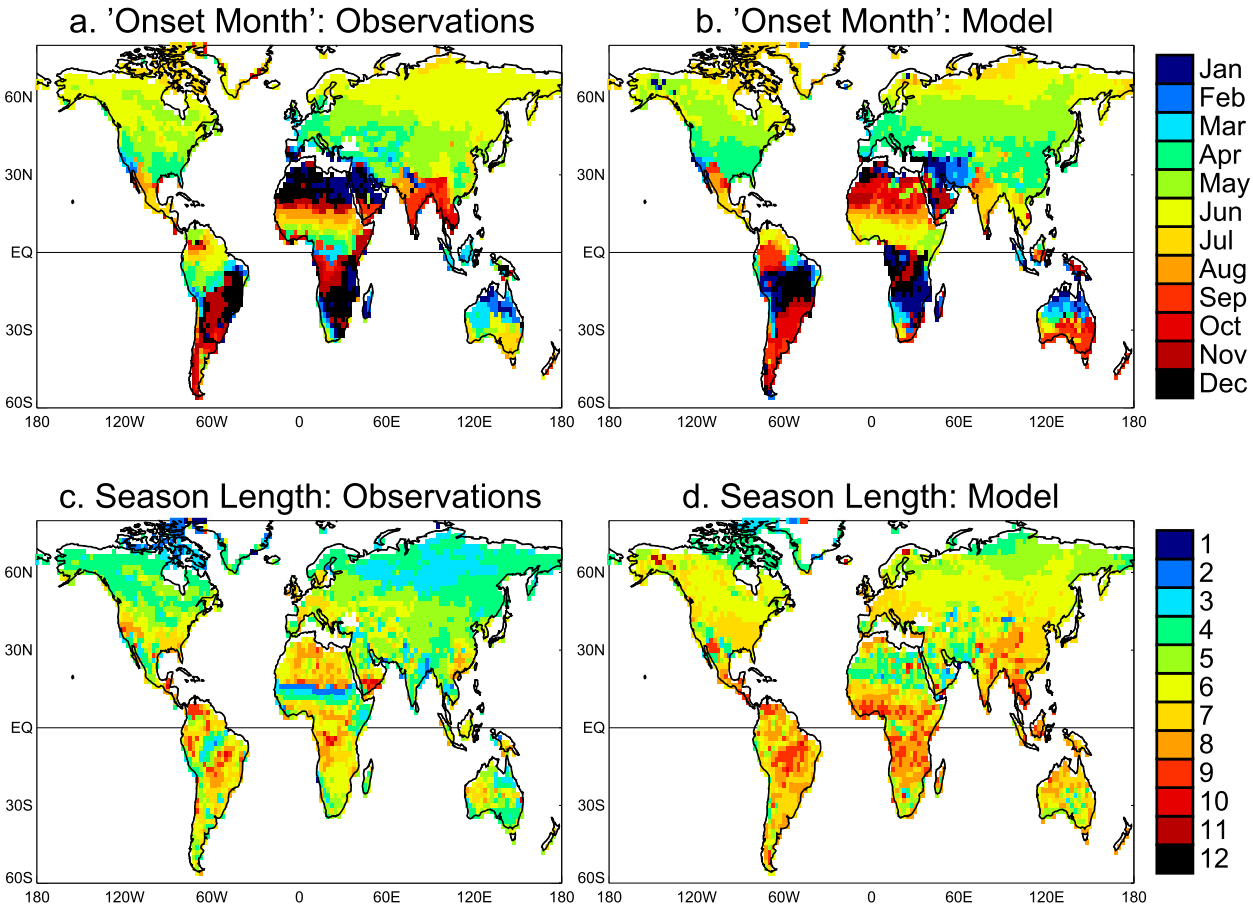

FIG. 6. (a) Onset month of the leafing-up cycle, loosely defined here as the first month of the mean seasonal FPAR cycle (from the observations-based GIMMS data) for which FPAR is in the upper half of the full annual range, on its climb to its maximum value. (b) As in (a), but for the simulation results. (c) FPAR season length, defined as the number of months for which the FPAR (from the observations-based GIMMS data) is in the upper half of its full annual range. (d) As in (c), but for the simulation results.

The agreement in spatial pattern with a presence of bias also manifests itself in the precipitation-based scatterplot in Fig. 5e and the corresponding binned version of the plot in Fig. 5f. In agreement with the observations, the model clearly shows an increase in FPAR with increasing precipitation and with decreasing precipitation variability. Overall, the model, though biased, does appear to simulate realistic controls of hydroclimatic variation over phenological means.

c. *Impact of hydrological variations on the interannual variability of phenological variables*

As a second and somewhat independent test of the ability of the Catchment-CN model to capture observed links between carbon and water variables, we examine the interannual variability of vegetation phenology. Rather than examining the total variance of a variable such as summertime NDVI, we focus instead on a modified quantity, one that captures the carbon–water connection,

$$\mathrm{Var(NDVI)}^* = \mathrm{Var(NDVI)Corr}^2\,(\mathrm{NDVI}, P), \quad (1)$$

where Var(NDVI) is the interannual variance of 3-month NDVI averages (again centered on the peak NDVI month, based on the climatological seasonal cycle), $\mathrm{Corr}^2(\mathrm{NDVI}, P)$ is the correlation between these individual NDVI averages and the corresponding yearly precipitation totals (with the end of the precipitation averaging period corresponding to the end of the 3-month NDVI averaging period), and Var(NDVI)* is interpreted as the portion of the NDVI variance associated with variations in moisture availability. That is, we are employing here the standard interpretation of $\mathrm{Corr}^2(\mathrm{NDVI}, P)$ as the fraction of the variance of NDVI *explained* by variations in P. Equation (1) allows us to isolate this part of NDVI variability from that associated with other sources, such as variations in radiation, nutrients, and temperature, as well as interference from clouds, water vapor, and aerosols (Los et al. 2000). [Note that Var(NDVI)* can also be expressed as the square of

the covariance between P and NDVI divided by the precipitation variance.]

A few notes are required regarding the estimation of Var(NDVI)*. First, by using the annual totals for precipitation, we are assuming that a given year's precipitation represents the water available that year for growth. Of course, other averaging periods for the precipitation could have been employed (e.g., Zeng et al. 2013). The patterns in $\mathrm{Corr}^2(\mathrm{NDVI}, P)$ obtained with these other averaging periods, however, turn out to be the same, to first order; correlation maps generated using 6- or 9-month precipitation averages (not shown) are very similar to those generated with the annual precipitation. Note that using the annual precipitation rather than the contemporaneous 3-month precipitation has an important advantage: it reflects that antecedent precipitation can provide water to vegetation growth through storage in ground reservoirs and snowpack (Milly 1994).

Second, the observations are known to be subject to significant contamination from clouds in high latitudes and from pollution (from biomass and fossil fuel burning) in Southeast Asia (Fensholt and Proud 2012): the upshot being that small and artifactual negative correlations between NDVI and precipitation are often seen in these regions. These negative correlations are problematic for our analysis. We zero them out before computing $\mathrm{Corr}^2(\mathrm{NDVI}, P)$, making the explicit assumption that any such negative correlations represent noise. Note that, even on the off chance that the negative correlations are real, they would not represent the physical relationship that we are after in this paper: namely, the ability of water limitations to limit vegetation growth.

Figure 7a shows the distribution of Var(NDVI)*, as computed with Eq. (1). The patterns are quite interesting: the regions for which moisture-related NDVI variability is high tend to coincide with the earth's grassland regimes—in the U.S. Great Plains, the Nordeste region of Brazil, the African Sahel, the Asian steppes, and eastern and northern Australia (see Fig. 8). The Var(NDVI)* patterns do miss grassland areas in India and China but, as shown in Fig. 8, these areas are subject to extensive irrigation (Siebert et al. 2005), a supply of water not accounted for in the $\mathrm{Corr}^2(\mathrm{NDVI}, P)$ diagnostic. Figure 7 demonstrates that, aside from such irrigated areas, the locations of the earth's grassland areas can be identified reasonably well from the joint analysis of NDVI and precipitation data. The same patterns and thus the same connections to grassland regimes are seen for Var(FPAR)*, the portion of the interannual variance in 3-month FPAR averages related to moisture variations.

The results obtained with the dynamic phenology model show very similar patterns. A comparison of Figs. 7b,c shows that the model captures very well the observed spatial pattern of Var(FPAR)*, though again with a bias, as indicated by the different scaling factors used for the plotting. Overall, the model successfully captures the role of hydroclimate in determining the spatial distribution of interannual variability in phenology.

4. Model experiments

Having demonstrated the Catchment-CN model's ability to capture the basic hydroclimatic controls on phenology seen in the observations, we now use model experiments to address key questions regarding the connections between hydroclimate and vegetation.

a. *Influence of vegetation type on phenological variability*

Clouding the interpretation of the Catchment-CN model's performance relative to observations in section 3 above is the possibility that its use of prescribed vegetation types is somehow guaranteeing correct model behavior. Given, for example, that the observed distribution of Var(FPAR)* in Fig. 7b captures well the locations of the world's grasslands (Fig. 8), we must consider the possibility that high values of Var(FPAR)* are encouraged by the unique properties of grassland and discouraged by the properties of forests and shrubs so that, by imposing the observed vegetation distributions in the model, we artificially guarantee high simulated values of Var(FPAR)* in the correct areas (Fig. 7c). The more intriguing possibility to consider, however, is that a specific hydroclimatic regime is responsible for high Var(FPAR)* values, a regime for which only grasslands happen to survive. With this second possibility, the vegetation type does not cause the Var(FPAR)* value; rather, the vegetation type and the Var(FPAR)* value are together controlled by something else, namely, the local moments of precipitation.

To examine this issue, we performed a repeat of the simulation described above but with a twist: grassland vegetation was imposed on all land surfaces, and no other vegetation types were allowed to exist. Thus, in this experiment, vegetation type could not affect in any way the simulated spatial and temporal distributions of FPAR. Note that, in this experiment, grassland is placed even in the driest deserts and in the wettest tropical areas; if the local climate is not conducive to grassland's survival, the grass is accordingly allowed to die out. Initial conditions for the all-grassland simulation were set everywhere to equilibrated states at a representative

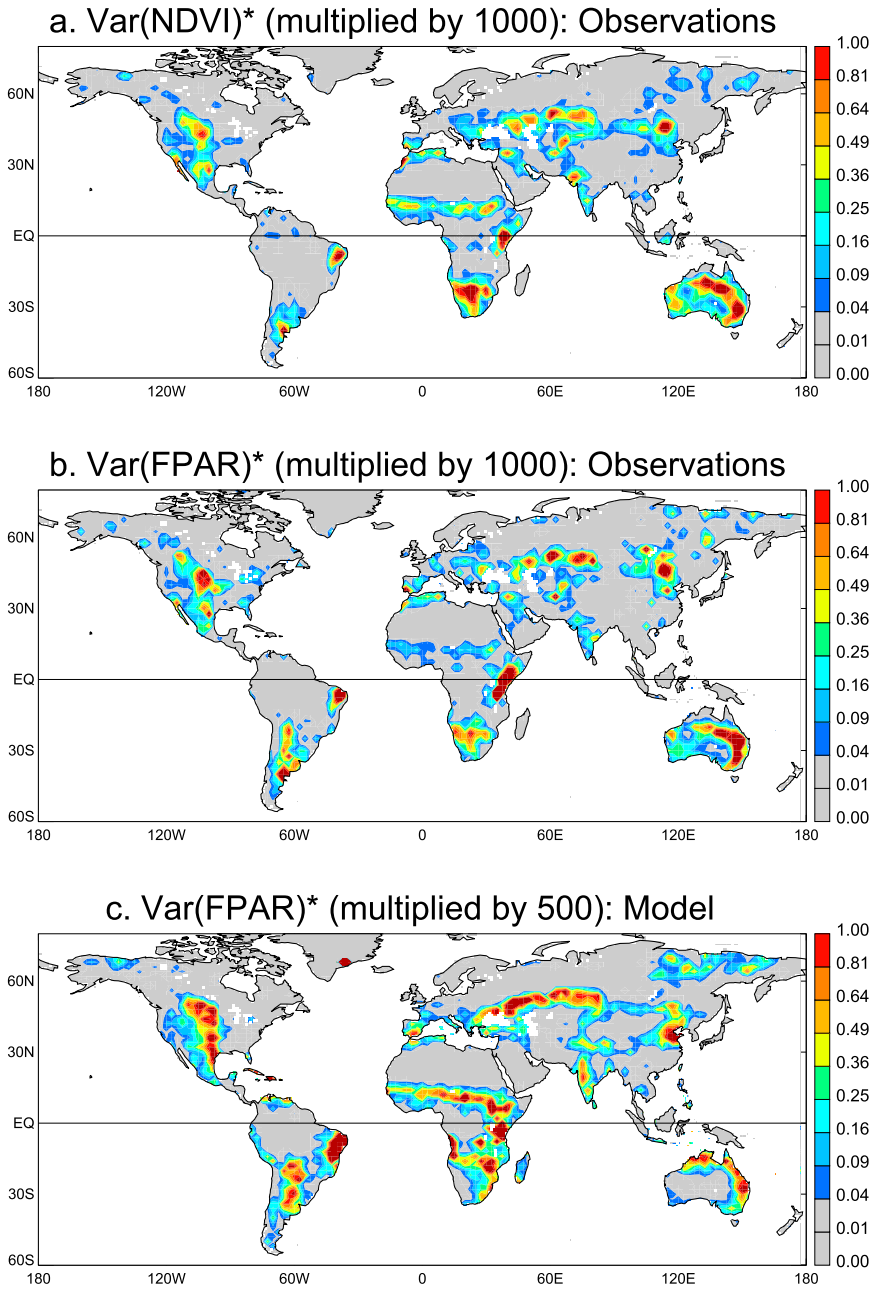

FIG. 7. (a) Product of the interannual variance of GIMMS NDVI data averaged over the maximum NDVI season and the square of the correlation between NDVI and annual precipitation, multiplied by 1000. (b) As in (a), but for GIMMS FPAR data. (c) As in (a), but for model-generated FPAR data and with the scaling factor changed to 500.

midlatitude grassland location, as extracted from the control simulation; the all-grassland simulation was then spun up for thirty-six 61-yr cycles prior to producing a final 61-yr cycle for analysis.

Figure 9c shows the spatial distribution of Var(FPAR)* for the all-grassland simulation. The plot captures, to first order, the features seen in the original model plot, supporting the second possibility noted above. (Note that differences between the control simulation and the all-grassland simulation in areas that are largely grassland in the control stem from details in the design of the all-grassland experiment, e.g., the use of the same nitrogen deposition rate across the globe.) That is, the presence of grassland does not lead to high Var(FPAR)*

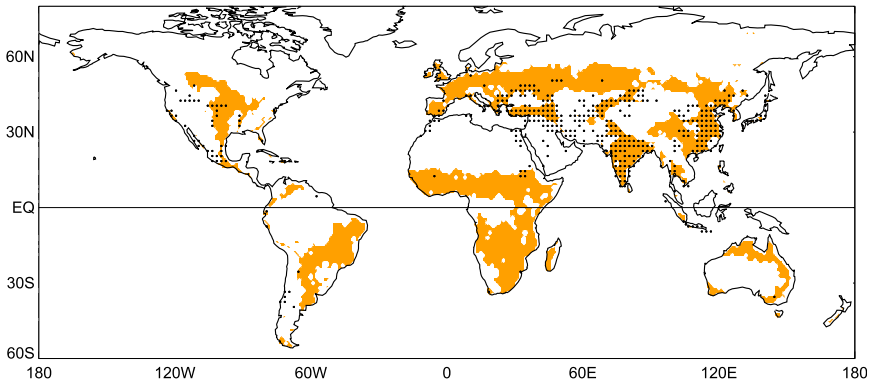

FIG. 8. Map of grassland locations, as derived from the distributions used in the second phase of the Global Soil Wetness Project (Dirmeyer et al. 2006). The dots overlain on the plot indicate regions for which irrigation is extensive [>10% of the land area, based on data aggregated from the Food and Agriculture Organization of the United Nations (FAO) http://www.fao.org/nr/water/aquastat/irrigationmap/index.stm], suggesting difficulty in relating observations-based FPAR values to local precipitation amounts.

values; the high values are, instead, indicative of a hydroclimatic regime that also happens to support grassland best. Similarly, the all-grassland simulation shows a relationship between FPAR maxima, mean precipitation, and precipitation variability (Fig. 9a) that agrees to first order with that seen in the original model simulation (Fig. 5f). That FPAR tends to be highest in very wet conditions, for example, is not simply the result of the presence of dense forests in wet areas; the wet conditions themselves encourage the high FPAR values, and wet areas also tend to be where dense forests tend to flourish.

We repeated the simulation still again, this time after prescribing a deciduous forest vegetation type everywhere (and spinning up the model for thirty-four 61-yr cycles). The results, shown in Figs. 9b,d, are essentially the same: the patterns, for example, in Var(FPAR)* for the all-grassland and all-trees cases are essentially identical. [There are, however, some intriguing differences between these simulations in the strength of the Var(FPAR)* field, with higher values for grassland in temperate regions and higher values for trees in tropical and subtropical regions.] Hydroclimatic variability, more than vegetation type, appears to dominate the spatial patterns of phenological variability: in the model and, we can infer, in nature.

b. *Hydroclimate and the global carbon cycle*

As noted in the introduction, a unique advantage of a model that can simulate phenology is its ability to provide information on additional, difficult to measure quantities. While carbon fluxes such as gross primary productivity (GPP), net primary productivity (NPP), and net ecosystem exchange (NEE) have been measured at various tower sites (Baldocchi 2008), directly observed global distributions of land–atmosphere carbon exchange are nonexistent. Model simulations, however, can readily provide these fields, and many examples of such simulated distributions already appear in the literature (e.g., Friedlingstein et al. 2006). [We note that other approaches for inferring global fields, such as machine learning algorithms that upscale from the site measurements, are also available (Jung et al. 2011).]

Here we provide model-based estimates of the connection between carbon exchange and hydroclimatic variability, focusing mainly on GPP. We first provide in Fig. 10a this particular model's vision of the global distribution of GPP. Because GPP is a flux rather than a manifestation of vegetation state, we present it in terms of annual averages rather than for a 3-month maximum period. The distributions have the expected maxima in the densely forested tropics, with swaths of high values in the boreal forests of the north. Figures 10b,c show the corresponding GPP fields from the simulations prescribing grassland and deciduous tree types, respectively. The three panels show some differences but are, to first order, very similar, indicating that vegetation type alone is not the main source of spatial variations in GPP; both GPP and vegetation distributions are apparently controlled in tandem by something else.

Naturally, that "something else" is water availability. Figure 11 shows, in analogy to Fig. 4, the square of the spatial correlation between GPP and various meteorological forcing variables, showing, in effect, which meteorological variables are statistically related to the GPP distribution and thus might have a hand in determining it. For all three simulations (control, all grass, and all trees), precipitation mean and variability have the

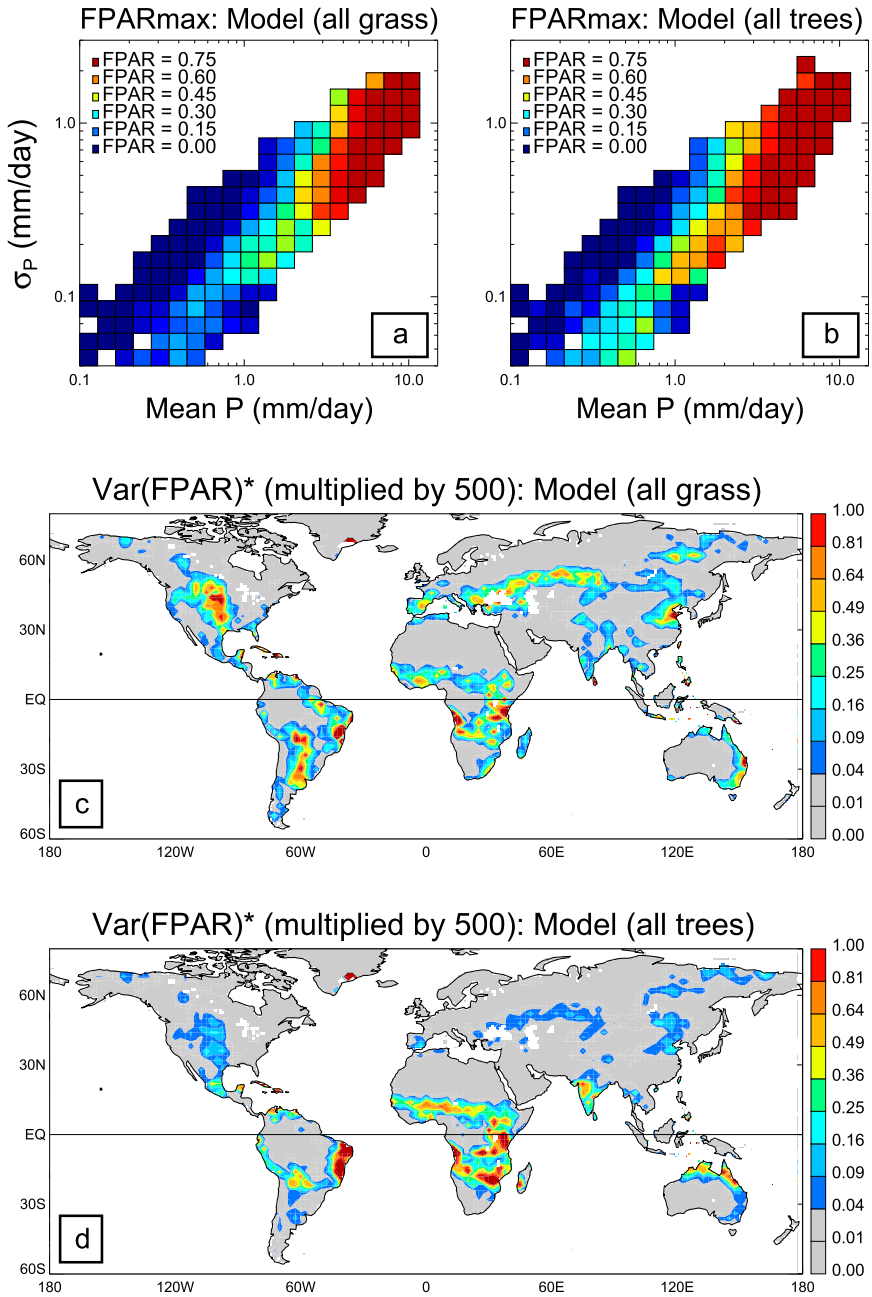

FIG. 9. (a) As in Fig. 5f (average model-simulated FPAR in peak FPAR season as a function of the mean precipitation and the standard deviation of annual precipitation), but for the case in which the entire globe is forced to be covered by grassland: (b) for the all-trees case. (c) As in Fig. 7c [product of the interannual variance of model-simulated FPAR (dimensionless) averaged over the maximum FPAR season and the square of the correlation between NDVI and annual precipitation, multiplied by 500], but for the case where the entire globe is forced to be covered by grassland: (d) for the all-trees case.

dominant impact on GPP, with an r^2 of about 0.55 for the multiple regression of GPP on $\log_{10}P$ and $\log_{10}\sigma_P$. Adding in the annual temperature, temperature deviation, and net radiation information increases the r^2 to about 0.64. The fact that the r^2 values do not increase by much for the uniform vegetation experiments suggests once again that variations in vegetation type do not by themselves contribute significantly to spatial variations in GPP; the remaining unexplained variance in Fig. 11a presumably results from spatial variability in, for

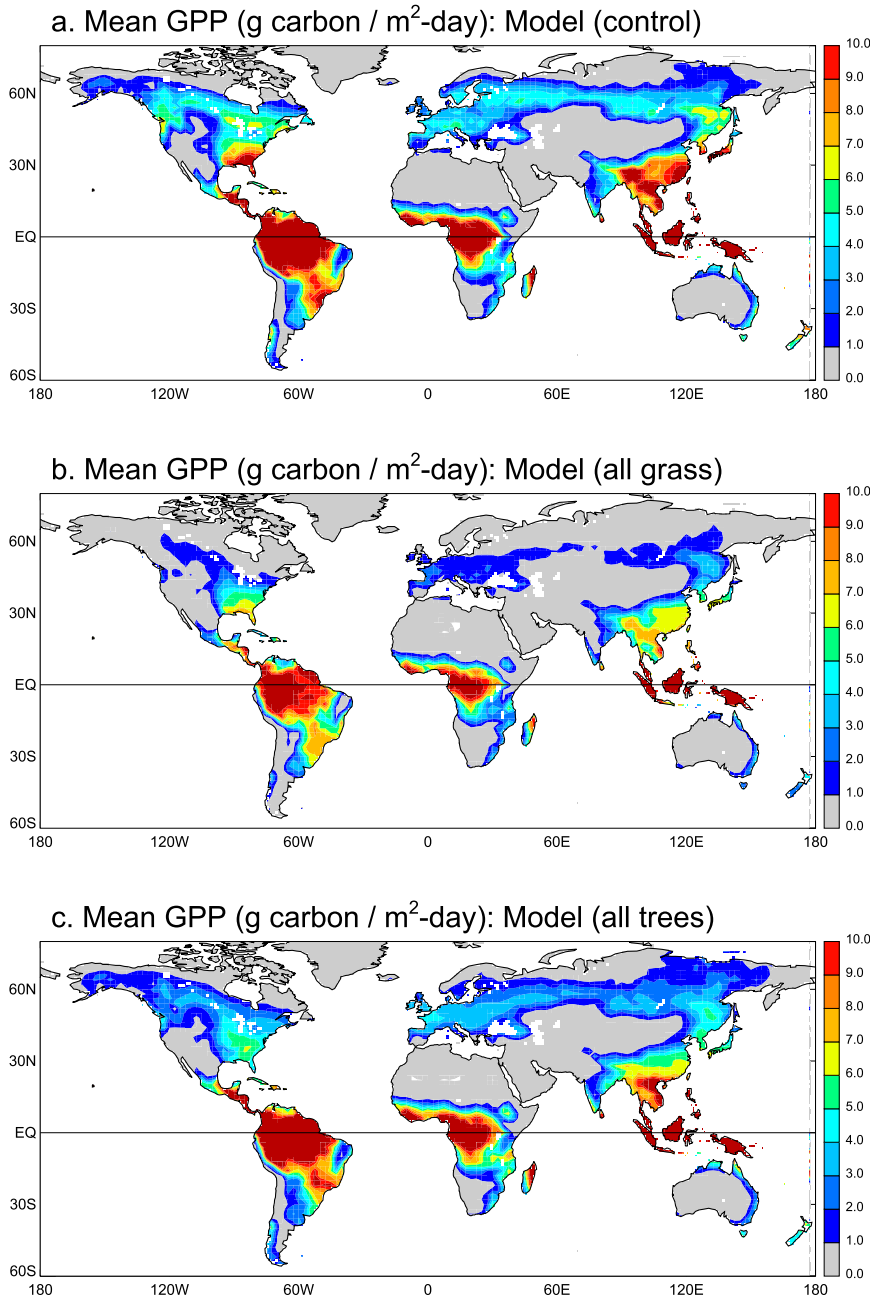

FIG. 10. Global distribution of annual GPP in grams of carbon per square meter per day ($gC\,m^{-2}\,day^{-1}$) for (a) the control simulation; (b) the simulation in which all land is covered with a grassland vegetation type; and (c) the simulation in which all land is covered with a deciduous tree vegetation type.

example, the seasonal cycles and shorter-term temporal structure of the forcing quantities.

Figure 12 shows how precipitation means and variability control the spatial distribution of GPP using scatterplots analogous to those shown in Fig. 5. As with FPAR, GPP tends to increase with increasing moisture availability (x axis) and decreasing interannual variability (y axis), regardless of which vegetation types are assigned at the surface.

In contrast to Fig. 5, Fig. 12 uses a nonlinear scale for the shading, a scale that shows the dominance of precipitation means over precipitation variability in determining GPP. The impact of precipitation variability on GPP, however, is nevertheless significant. This is

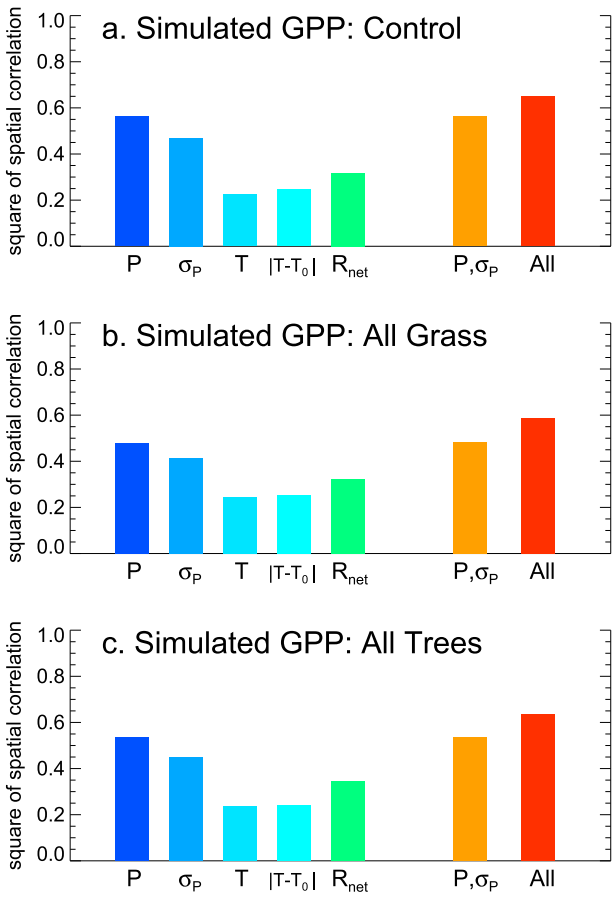

FIG. 11. (a) As in Fig. 4, but for annual GPP (rather than year-high NDVI or FPAR) produced in the control simulation. Annual temperatures are used for the third bar, whereas warmest-month temperature deviations from a single optimal temperature (as in Fig. 4) are used for the fourth bar. The optimal temperature (T_0) is set here to 299 K, which for this exercise turns out to maximize the height of the bar. (b),(c) As in (a), but for GPP produced (b) in the all-grass simulation and (c) in the all-trees simulation.

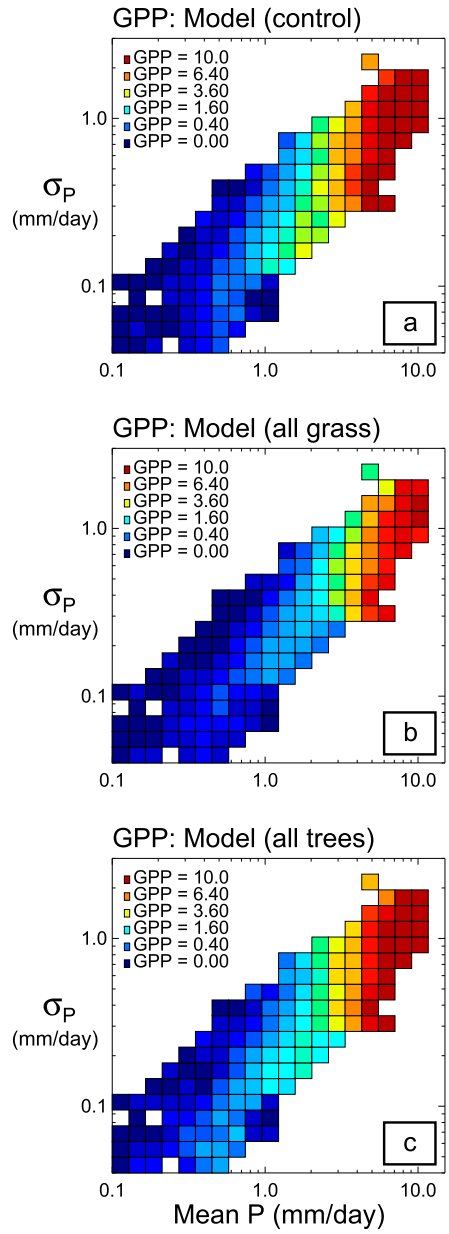

FIG. 12. (a) Average annual GPP ($gC\,m^{-2}\,day^{-1}$) as a function of the mean precipitation (x coordinate) and the standard deviation of annual precipitation (y coordinate) in the control simulation, with individual land grid cell values averaged over bins. At least five dots must lie within a bin for the binned value to be plotted. (b),(c) As in (a), but for the simulation in which all land is covered (b) with a grassland vegetation type and (c) with a deciduous tree vegetation type.

demonstrated with a supplemental model simulation ("ClimP") in which we prescribed standard, spatially varying vegetation types (as in the control simulation) but a modified precipitation forcing: at each grid cell in ClimP, we scaled the precipitation forcing in each month of each year so that the seasonal cycle of monthly totals for the year matched the long-term (climatological) seasonal cycle. Thus, in ClimP, we artificially removed the monthly-scale year-to-year temporal variability in the precipitation forcing—at each grid cell, the mean precipitation applied was identical to that used in the control simulation, whereas the interannual variability of monthly precipitation was, by construction, set to zero.

Figure 13 shows the difference between the mean annual GPP produced in ClimP and that in the control simulation. Regions with large positive differences appear in the southeast United States, along the eastern coasts of South America and Australia, in the Indian subcontinent, in northeastern China, and in various other regions of South America and Africa. Negative differences do not appear anywhere. In effect, Fig. 12 illustrates where GPP in the real world would be larger if the year-to-year precipitation supply were more

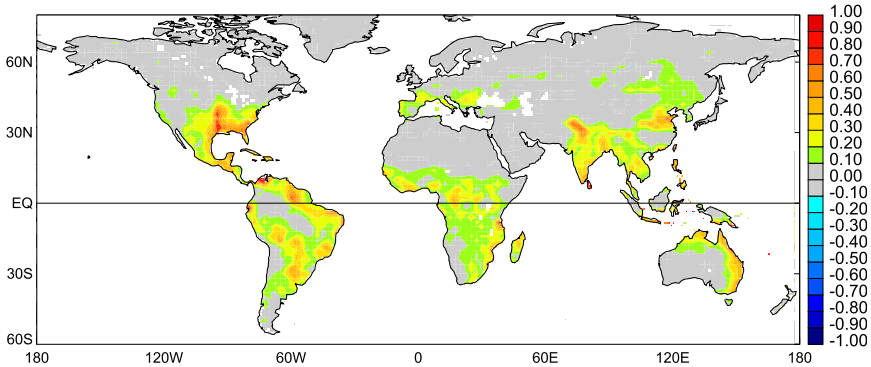

FIG. 13. Difference in the mean annual GPP ($gC\,m^{-2}\,day^{-1}$) produced in the ClimP simulation (the simulation using climatological precipitation forcing) and that produced in the control simulation.

dependable: that is, where the interannual variability of precipitation holds down the land surface's carbon uptake. Note, however, that human activities can mitigate the effects of this variability. India, Southeast Asia, and northeastern China in particular are known to undergo extensive irrigation (Fig. 8). Because irrigation is effectively a means of providing a more dependable water supply, these particular areas may, in the real world, be capturing the larger GPP rates.

With Fig. 14, we focus on the interannual variability of GPP at each grid cell rather than on the spatial distribution of its mean. Figure 14a shows the variance of annual GPP. Figure 14b shows the spatial distribution of $Corr^2(GPP, P)$, where P is the annual precipitation; that is, Fig. 14b shows the fraction of the total GPP variance that is associated with, or can be explained by, variations in annual water supply. The fractions are reasonably large across the globe, even in some areas considered to be not strongly water stressed, such as the southeastern United States. In contrast, the fields of $Corr^2(GPP, T)$ and $Corr^2(GPP, R_{net})$, where T is the yearly averaged temperature and R_{net} is the yearly averaged net radiation, show significantly lower values (Figs. 14c,d). While interannual temperature variations do have some impact on high latitude GPP variations (perhaps through their effects on snow cover duration), they have much smaller impact elsewhere. [Note that, when May–September average temperatures are used (not shown) rather than annual temperatures, the $Corr^2(GPP, T)$ values do increase significantly in many Northern Hemisphere temperate regions, though still not to the level of the indicated $Corr^2(GPP, P)$ values.] Interannual net radiation variations appear to contribute more, especially in Africa; it is quite possible, however, that these particular contributions are not real and instead simply reflect known existing correlations between precipitation and net radiation there (not shown).

Together, annual precipitation, temperature, and net radiation do not explain all of the simulated GPP variability. As before, presumably a significant part of the variability stems from year-to-year variations in, for example, the subannual timing of the precipitation and associated variations in infiltration and runoff.

Figure 15 shows one final interesting result regarding the interannual variability of GPP. The shading shows Var(GPP) for a 3-month averaging period (centered, at each grid cell, around the month of maximum GPP). Overlain on the plot are black dots indicating where Var(FPAR) for 3-month averages (centered around the local monthly maximum for FPAR) exceeds a value of 0.003, an arbitrary threshold chosen for plotting convenience. The figure shows that Var(GPP) and Var(FPAR) tend not to be maximized in the same regions; Var(GPP) maxima tend to lie on the wetter sides of the Var(FPAR) maxima. The same basic result (not shown) is found for comparisons of the water-limited portions of the variances [i.e., Var(GPP)* versus Var(FPAR)*], and it is also found (not shown) for the all-grassland and all-deciduous-trees simulations, suggesting that variations in vegetation type are not responsible for such spatial offsets in the maxima. The spatial offsets are instead induced by the carbon physics built into the modeling system. Assuming these physical treatments are accurate, then similar offsets would apply to the real world's distributions of Var(GPP) and Var(FPAR). In other words, given estimates of Var(FPAR) attained, for example, through the processing of the GIMMS data, knowledge of the offsets could potentially help in the construction of an estimated spatial field of Var(GPP).

5. Summary and discussion

Using the Catchment-CN model, a merger of the dynamic phenology components of the CLM4 dynamic

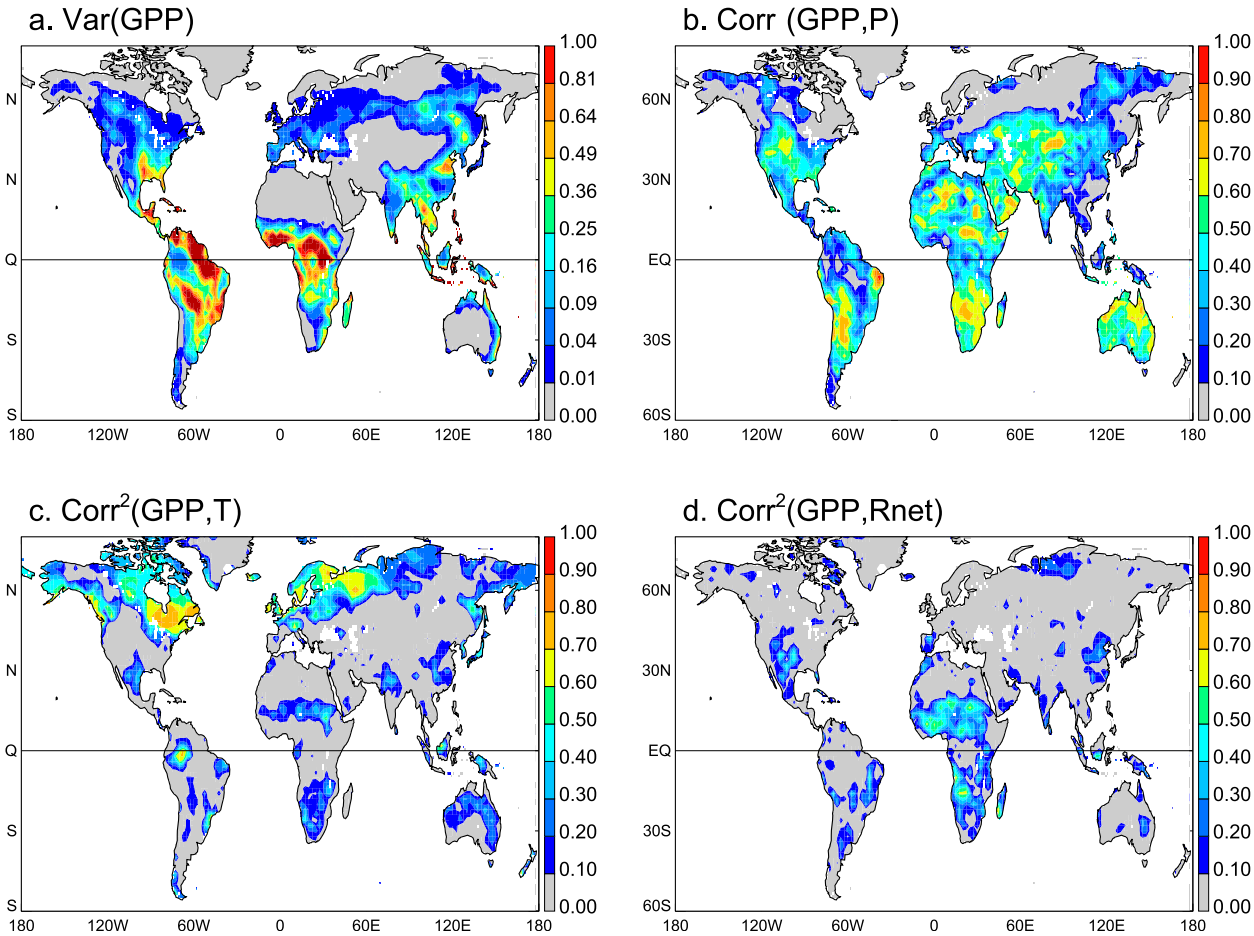

FIG. 14. (a) Variance of annual GPP ($g^2\,m^{-4}\,day^{-2}$) as produced by the control simulation. (b) $Corr^2$(GPP, *P*): that is, the fraction of the GPP variance associated with interannual variations in annual precipitation. (c),(d) As in (b), but for the fraction of the GPP variance associated with interannual variations in (c) annual temperature and (d) annual net radiation.

vegetation model with the water and energy budget framework of the GMAO catchment LSM, we examine the connections across the globe between hydroclimate and vegetation variables. Justification for the use of this model in such a study is provided by its demonstrated ability to reproduce observed connections between FPAR and precipitation moments (section 3): namely, the increase in FPAR with increasing mean precipitation

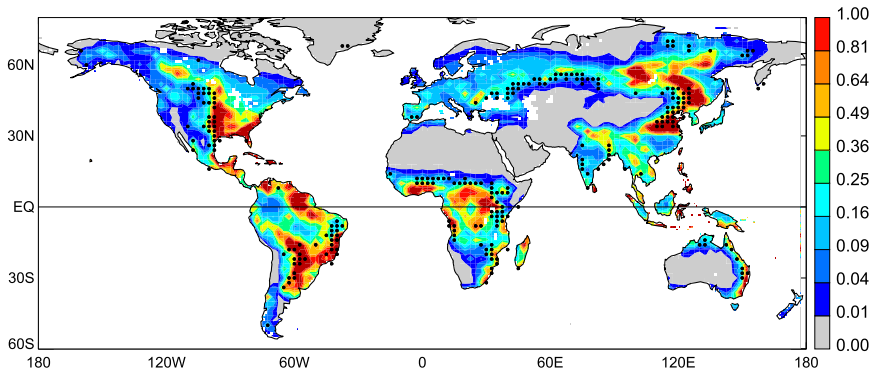

FIG. 15. Interannual variance of GPP ($g^2\,m^{-4}\,day^{-2}$) for the 3-month period centered on the month for which the local GPP is climatologically largest. Overlain on the plot are black dots showing where the interannual variance of 3-month FPAR is maximized.

and decreasing precipitation variability and the proper geographical placement of spatial maxima in the global field of moisture-related FPAR variance.

Our model results can be summarized as follows. First, based on our supplemental simulations with globally uniform vegetation type, we find that the aforementioned relationships between FPAR and precipitation moments are largely independent of vegetation type; the fact that trees grow in wet regimes, grass grows in drier regimes, and shrubs grow in even drier regimes has only a second-order impact on the spatial distribution of FPAR and its interannual variability at each location. Instead, hydroclimatic moments appear to be the dominant determinants of both vegetation type and phenological expression, as represented by FPAR. Our second basic result is that hydroclimatic moments provide a similarly dominant control over the spatial and temporal variability of gross primary productivity (GPP), again with only a second-order contribution from vegetation type.

Such a global-scale description of GPP connections to hydroclimate is achievable with a DVM but is not possible with observations, which are much more spatially and temporally limited. Knapp and Smith (2001) used observations collected across 11 tower sites to show that above-ground net primary production (ANPP) tends to increase with increasing annual precipitation, and our global-scale results (for GPP, a related variable) are consistent with this. We do see some inconsistencies, however, with their study. For example, Knapp and Smith find that ANPP has its maximum interannual variability in grassland areas. We find that, while the interannual variability of FPAR is maximized in grassland areas, the maxima for GPP variability tend to be spatially offset from these FPAR variance maxima (Fig. 15), slightly toward the wetter (forested) side. The offset is minor, however, and the apparent inconsistency, while certainly a possible result of model deficiencies, may also relate to the limited number of tower sites they examined. More importantly, Knapp and Smith (2001) find that "interannual variability in ANPP [is] not related to variability in precipitation" (p. 481). Results from our control simulation (not shown) indicate that the square of the spatial correlation coefficient between Var(GPP) and Var(P) across land points is on the order of 30%, which disagrees with their conclusion; indeed, when we limit the calculation to values at the grid cells containing the Long-Term Ecological Research (LTER) sites they studied, the square of the correlation coefficient increases. We also find a reasonably strong relationship between the time series of GPP and precipitation (Fig. 14b) at individual locations.

While interpretations of DVM-based results must be tempered by knowledge of model biases and limitations, DVM experiments, if properly interpreted, open the door to a wealth of potential studies of the global carbon cycle and its interactions with the global water and energy cycles. This paper provides one such study. Another example of note is provided by Guan et al. (2012), who show with DVM simulations over Africa that the statistical character of precipitation forcing (e.g., rainfall intensity) manifests itself in the GPP produced. The advantages of using DVMs—their provision of comprehensive (and often unmeasurable) data and their ability to be modified at will to allow the examination of the impacts of individual physical processes—stand them in good stead for future carbon analyses. Our understanding of global carbon–water–energy connections should continue to increase as researchers continue to improve their models through careful analysis against observations (Luo et al. 2012) and apply them to carbon–water–energy questions in innovative ways.

Acknowledgments. This research was supported by the NASA Modeling, Analysis, and Prediction Program.

REFERENCES

Adler, R. F., G. J. Huffman, and P. R. Keehn, 1994: Global tropical rain estimates from microwave-adjusted geosynchronous IR data. *Remote Sens. Rev.,* **11,** 125–152, doi:10.1080/02757259409532262.

——, and Coauthors, 2003: The Version-2 Global Precipitation Climatology Project (GPCP) monthly precipitation analysis (1979–present). *J. Hydrometeor.,* **4,** 1147–1167, doi:10.1175/1525-7541(2003)004<1147:TVGPCP>2.0.CO;2.

Baldocchi, D., 2008: "Breathing" of the terrestrial biosphere: Lessons learned from a global network of carbon dioxide flux measurement systems. *Aust. J. Bot.,* **56,** 1–26, doi:10.1071/BT07151.

Beck, H. E., T. R. McVicar, A. I. J. M. van Dijk, J. Schellekens, R. A. M. de Jeu, and L. A. Bruijnzeel, 2011: Global evaluation of four AVHRR-NDVI data sets: Intercomparison and assessment against Landsat imagery. *Remote Sens. Environ.,* **115,** 2547–2563, doi:10.1016/j.rse.2011.05.012.

Berry, J. A., D. J. Beerling, and P. J. Franks, 2010: Stomata: Key players in the earth system, past and present. *Curr. Opin. Plant Biol.,* **13,** 232–240, doi:10.1016/j.pbi.2010.04.013.

Boussetta, S., and Coauthors, 2013: Natural land carbon dioxide exchanges in the ECMWF integrated forecasting system: Implementation and offline validation. *J. Geophys. Res. Atmos.,* **118,** 5923–5946, doi:10.1002/jgrd.50488.

Bowling, D. R., S. Bethers-Marchetti, C. K. Lunch, E. E. Grote, and J. Belnap, 2010: Carbon, water, and energy fluxes in a semiarid cold desert grassland during and following multiyear drought. *J. Geophys. Res.,* **115,** G04026, doi:10.1029/2010JG001322.

Budyko, M. I., 1974: *Climate and Life.* Academic Press, 508 pp.

Choudhury, B., 1987: Relationships between vegetation indices, radiation, absorption, and net photosynthesis evaluated by a sensitivity analysis. *Remote Sens. Environ.,* **22,** 209–233, doi:10.1016/0034-4257(87)90059-9.

Dirmeyer, P. A., X. Gao, M. Zhao, Z. Guo, T. Oki, and N. Hanasaki, 2006: GSWP-2 multimodel analysis and implications for our

perception of the land surface. *Bull. Amer. Meteor. Soc.,* **87,** 1381–1397, doi:10.1175/BAMS-87-10-1381.

Dunne, J. P., and Coauthors, 2013: GFDL's ESM2 global coupled climate–carbon Earth system models. Part II: Carbon system formulation and baseline simulation characteristics. *J. Climate,* **26,** 2247–2267, doi:10.1175/JCLI-D-12-00150.1.

Fang, J., S. Piao, L. Zhou, J. He, F. Wei, R. B. Myneni, C. J. Tucker, and K. Tan, 2005: Precipitation patterns alter growth of temperate vegetation. *Geophys. Res. Lett.,* **32,** L21411, doi:10.1029/2005GL024231.

Fensholt, R., and S. R. Proud, 2012: Evaluation of Earth Observation based global long term vegetation trends—Comparing GIMMS and MODIS global NDVI time series. *Remote Sens. Environ.,* **119,** 131–147, doi:10.1016/j.rse.2011.12.015.

Friedlingstein, P., and Coauthors, 2006: Climate–carbon cycle feedback analysis: Results from the C^4MIP model intercomparison. *J. Climate,* **19,** 3337–3353, doi:10.1175/JCLI3800.1.

Goward, S. N., and K. F. Huemmrich, 1992: Vegetation canopy PAR absorptance and the normalized difference vegetation index: An assessment using the SAIL model. *Remote Sens. Environ.,* **39,** 119–140, doi:10.1016/0034-4257(92)90131-3.

Guan, K., E. F. Wood, D. Medvigy, K. K. Caylor, S. S. Good, and J. Sheffield, 2012: Quantify the impacts of seasonal variability in precipitation on vegetation functions in Africa. *2012 Fall Meeting,* San Francisco, CA, Amer. Geophys. Union, Abstract B53A-0655.

Hall, F. G., and Coauthors, 2006: ISLSCP Initiative II global data sets, Surface boundary conditions and atmospheric forcings for land-atmosphere studies. *J. Geophys. Res.,* **111,** D22S01, doi:10.1029/2006JD007366.

Ichii, K., A. Kawabata, and Y. Yamaguchi, 2002: Global correlation analysis for NDVI and climatic variables and NDVI trends: 1982-1990. *Int. J. Remote Sens.,* **23,** 3873–3878, doi:10.1080/01431160110119416.

Jahan, N., and T. Y. Gan, 2011: Modelling the vegetation-climate relationship in a boreal mixedwood forest of Alberta using normalized difference and enhanced vegetation indices. *Int. J. Remote Sens.,* **32,** 313–335, doi:10.1080/01431160903464146.

Jung, M., and Coauthors, 2011: Global patterns of land-atmosphere fluxes of carbon dioxide, latent heat, and sensible heat derived from eddy covariance, satellite, and meteorological observations. *J. Geophys. Res.,* **116,** G00J07, doi:10.1029/2010JG001566.

Kaufman, Y. J., D. D. Herring, K. J. Ranson, and G. J. Collatz, 1998: Earth Observing System AM1 mission to Earth. *IEEE Trans. Geosci. Remote Sens.,* **36,** 1045–1055, doi:10.1109/36.700989.

Knapp, A. K., and M. D. Smith, 2001: Variation among biomes in temporal dynamics of aboveground primary production. *Science,* **291,** 481–484, doi:10.1126/science.291.5503.481.

Kobe, R. K., 1997: Carbohydrate allocation to storage as a basis of interspecific variation in sapling survivorship and growth. *Oikos,* **80,** 226–233, doi:10.2307/3546590.

Koster, R. D., M. J. Suarez, A. Ducharne, M. Stieglitz, and P. Kumar, 2000: A catchment-based approach to modeling land surface processes in a general circulation model: 1. Model structure. *J. Geophys. Res.,* **105,** 24 809–24 822, doi:10.1029/2000JD900327.

Krinner, G., and Coauthors, 2005: A dynamic global vegetation model for studies of the coupled atmosphere-biosphere system. *Global Biogeochem. Cycles,* **19,** GB1015, doi:10.1029/2003GB002199.

Lawrence, D. M., and Coauthors, 2011: Parameterization improvements and functional and structural advances in version 4 of the Community Land Model. *J. Adv. Model. Earth Syst.,* **3,** M03001, doi:10.1029/2011MS000045.

Leuning, R., and Coauthors, 2004: Spatial and temporal variations in fluxes of energy, water vapour, and carbon dioxide during OASIS 1994 and 1995. *Bound.-Layer Meteor.,* **110,** 3–38, doi:10.1023/A:1026028217081.

Los, S. O., and Coauthors, 2000: A global 9-yr biophysical land surface dataset from NOAA AVHRR data. *J. Hydrometeor.,* **1,** 183–199, doi:10.1175/1525-7541(2000)001<0183:AGYBLS>2.0.CO;2.

Luo, Y. Q., and Coauthors, 2012: A framework for benchmarking land models. *Biogeosciences,* **9,** 3857–3874, doi:10.5194/bg-9-3857-2012.

Milly, P. C. D., 1994: Climate, soil water storage, and the average annual water balance. *Water Resour. Res.,* **30,** 2143–2156, doi:10.1029/94WR00586.

Moore, I. D., A. Lewis, and J. C. Gallant, 1993: Terrain attributes, estimation methods and scale effects. *Modeling Change in Environmental Systems,* A. J. Jakeman, M. B. Beck, and M. McAleer, Eds., Wiley, 189–214.

Oleson, K. W., and Coauthors, 2010: Technical description of version 4.0 of the Community Land Model (CLM). NCAR Tech. Note NCAR/TN-478+STR, 257 pp.

Puma, M. J., R. D. Koster, and B. I. Cook, 2013: Phenological versus meteorological controls on land-atmosphere water and carbon fluxes. *J. Geophys. Res. Biogeosci.,* **118,** doi:10.1029/2012JG002088.

Randerson, J. T., and Coauthors, 2009: Systematic assessment of terrestrial biogeochemistry in coupled climate–carbon models. *Global Change Biol.,* **15,** 2462–2484, doi:10.1111/j.1365-2486.2009.01912.x.

Sellers, P. J., C. J. Tucker, G. J. Collatz, S. O. Los, C. O. Justice, D. A. Dazlich, and D. A. Randall, 1996: A revised land surface parameterization (SiB2) for atmospheric GCMs. Part II: The generation of global fields of terrestrial biophysical parameters from satellite data. *J. Climate,* **9,** 706–737, doi:10.1175/1520-0442(1996)009<0706:ARLSPF>2.0.CO;2.

——, and Coauthors, 1997: Modeling the exchanges of energy, water, and carbon between continents and the atmosphere. *Science,* **275,** 502–509, doi:10.1126/science.275.5299.502.

Sheffield, J., G. Goteti, and E. F. Wood, 2006: Development of a 50-year high-resolution global dataset of meteorological forcings for land surface modeling. *J. Climate,* **19,** 3088–3111, doi:10.1175/JCLI3790.1.

Shi, M. J., Z.-L. Yang, D. M. Lawrence, R. E. Dickinson, and Z. M. Subin, 2013: Spin-up processes in the Community Land Model version 4 with explicit carbon and nitrogen components. *Ecol. Modell.,* **263,** 308–325, doi:10.1016/j.ecolmodel.2013.04.008.

Siebert, S., P. Doll, J. Hoogeveen, J. M. Faures, K. Frenken, and S. Feick, 2005: Development and validation of the global map of irrigation areas. *Hydrol. Earth Syst. Sci.,* **9,** 535–547, doi:10.5194/hess-9-535-2005.

Thornton, P. E., and Coauthors, 2009: Carbon-nitrogen interactions regulate climate-carbon cycle feedbacks: Results from an atmosphere-ocean general circulation model. *Biogeosciences,* **6,** 2099–2120, doi:10.5194/bg-6-2099-2009.

Trenberth, K. E., J. T. Fasullo, and J. Mackaro, 2011: Atmospheric moisture transports from ocean to land and global energy flows in reanalyses. *J. Climate,* **24,** 4907–4924, doi:10.1175/2011JCLI4171.1.

Tucker, C. J., J. E. Pinzon, M. E. Brown, D. A. Slayback, E. W. Pak, R. Mahoney, E. F. Vermote, and N. El Saleous, 2005: An extended AVHRR 8-km NDVI dataset compatible with

MODIS and SPOT vegetation NDVI data. *Int. J. Remote Sens.,* **26,** 4485–4498, doi:10.1080/01431160500168686.

Wang, G., and E. A. B. Eltahir, 2000: Biosphere–atmosphere interactions over West Africa. II: Multiple climate equilibria. *Quart. J. Roy. Meteor. Soc.,* **126,** 1261–1280, doi:10.1002/qj.49712656504.

White, M. A., P. E. Thornton, and S. W. Running, 1997: A continental phenology model for monitoring vegetation responses to interannual climatic variability. *Global Biogeochem. Cycles,* **11,** 217–234, doi:10.1029/97GB00330.

Zeng, F.-W., G. J. Collatz, J. E. Pinzon, and A. Ivanoff, 2013: Evaluating and quantifying the climate-driven interannual variability in Global Inventory Modeling and Mapping Studies (GIMMS) Normalized Difference Vegetation Index (NDVI3g) at global scales. *Remote Sens.,* **5,** 3918–3950, doi:10.3390/rs5083918.

Zeng, N., J. D. Neelin, K.-M. Lau, and C. J. Tucker, 1999: Enhancement of interdecadal climate variability in the Sahel by vegetation interaction. *Science,* **286,** 1537–1540, doi:10.1126/science.286.5444.1537.